Nano Research

Open Access

Research Article

Efficient high-entropy alloy electrocatalyst by rapid microwave synthesis for glycerol-assisted hydrogen evolution

Jietao Jiang[1,2], Fengfei Xu[1], Wenzhuo Zhang[2], Zheng Chen[2], Xinqi Wu[2], Xiaoyu Liu[1], Lijun Yang[1], Qiang Wu[1] ✉, Xizhang Wang[1] ✉, and Zheng Hu[1]

[1] *Key Laboratory of Mesoscopic Chemistry of Ministry of Education (MOE), Jiangsu Provincial Laboratory for Nanotechnology, School of Chemistry and Chemical Engineering, Nanjing University, Nanjing 210023, China*
[2] *School of Metallurgical Engineering, Jiangxi University of Science and Technology, Ganzhou 341000, China*

Cite this article: *Nano Research*, **2026**, *19*, 94908651. https://doi.org/10.26599/NR.2026.94908651

ABSTRACT: Electrochemical glycerol oxidation reaction (GOR) is an attractive alternative reaction to oxygen evolution reaction (OER) of water electrolysis due to the lower oxidation potential and value-added oxidation products. Developing high-efficient bifunctional electrocatalysts toward anodic GOR and cathodic hydrogen evolution reaction (HER) still faces a grand challenge. Herein, we have constructed high-entropy alloy (HEA) nanoparticles supported on hierarchical N-doped carbon nanocages (hNCNC) by a facile and rapid microwave synthesis. The optimal catalyst exhibits excellent performance in the glycerol-assisted water electrolysis, with an ultralow cell voltage of 0.373 V at 10 mA·cm^{-2} and a long-term stability over 50 h with nearly 100% Faradaic efficiency for H_2. The superior performance is ascribed to the increased capability of C–C cleavage and anti-poisoning for GOR and the multiple active sites for HER due to the high-entropy effect, as well as high dispersion and enhanced stability of HEA nanoparticles on hNCNC. This study not only demonstrates an effective approach for constructing advanced bifunctional electrocatalysts for GOR and HER, but also provides new ideas for energy-efficient hydrogen generation by glycerol-assisted water electrolysis

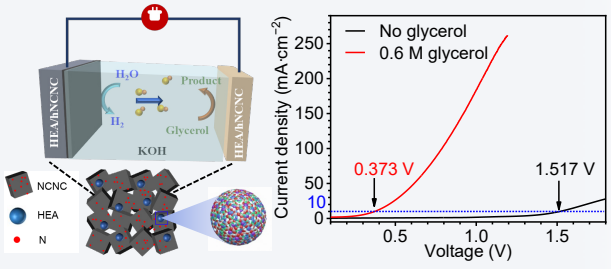

KEYWORDS: high-entropy alloy, microwave synthesis, hydrogen evolution reaction, water splitting, glycerol oxidation reaction

1 Introduction

Molecular hydrogen is an ideal energy carrier for addressing the increasing energy and environmental challenges in virtue of its sustainability, net-zero emission, and high energy density [1, 2]. Water electrolysis is a sustainable approach for hydrogen production in comparison with traditional methane/methanol reforming [3–5]. However, the cell voltage of water electrolyzer is much higher than the theoretical value (1.229 V) mainly due to the sluggish kinetics of anodic oxygen evolution reaction (OER), resulting in low energy conversion efficiency and high cost to limit its large-scale application [6, 7]. An attractive solution is to replace the OER with electrooxidation reactions of small molecules that possess lower oxidation potentials (such as ethanol [8], benzyl alcohol [9–11], urea [12, 13], amine [14], hydrazine [15], and glucose [16]). Glycerol, a by-product of biodiesel production industry, shows much lower theoretical oxidation potential (0.003 V vs. reversible hydrogen electrode (RHE)) than OER and lower cost than other small molecules [17, 18]. Glycerol can be oxidized into valuable chemicals with broad applications, such as lactic acid, dihydroxyacetone, glyceric acid, glycolic acid, and formic acid [19–21]. In view of this, glycerol-assisted water splitting by coupling glycerol oxidation reaction (GOR) with hydrogen evolution reaction (HER) holds great promise in reducing energy barriers associated with OER.

Currently, Pt catalyst is the most popular electrocatalyst for GOR and HER due to the lower overpotential and higher activity [4, 22]. Unfortunately, Pt suffers from susceptibility to poisoning and inadequate capability of C–C cleavage during GOR, as well as the scarce resource and high price [23, 24]. Hence, it is significant to develop the bifunctional electrocatalyst for glycerol-assisted water splitting with low cost, high activity, and robust anti-poisoning capability. High-entropy alloys (HEAs) have been garnering more

Received: December 19, 2025; **Revised:** March 15, 2026
Accepted: March 18, 2026

✉Address correspondence to Qiang Wu, wqchem@nju.edu.cn; Xizhang Wang, wangxzh@nju.edu.cn

and more attention owing to their distinctive and fascinating properties compared to traditional alloys, demonstrating great potential applications in various fields [25, 26]. Some HEAs, particularly Pt-based HEAs, are very suitable to catalyze GOR and HER because their multiple active sites can boost the oxidation of various intermediates involved in GOR and improve the adsorption/desorption of *H intermediates in HER [27–30]. Moreover, introducing other metals into HEA catalysts can reduce the Pt usage and regulate the electronic structure and intrinsic catalytic activity. To date, HEAs have been developed by various synthetic methods, such as wet-chemical synthesis, ball milling, sputtering deposition, and pyrolysis, which, however, were troubled by the challenges of high energy consumption, or difficulty of size control, or complex preparation process, or easy element segregation [31, 32]. Therefore, it is highly desired to explore eco-friendly, facile, and size-controllable preparation methods for HEA catalysts. The microwave synthesis boasts high efficiency, energy savings, and adjustable power, becoming an ideal choice for preparing carbon-supported catalysts [33–35].

Here, we have prepared a bifunctional catalyst by loading PtRhRuCuCrMn HEA nanoparticles on hierarchical N-doped carbon nanocages (HEA/hNCNC) through a facile and rapid microwave synthesis. The constituent elements of PtRhRuCuCrMn HEA were selected due to the following motivations: (i) Pt serves as main active component for both GOR and HER; (ii) Rh and Cu can enhance the C–C cleavage in GOR [23, 36]; and (iii) oxophilic metals of Ru, Cr, and Mn can weaken the binding strength of *CO to promote its oxidation during GOR, and optimize OH-binding as well as H-binding energies to facilitate HER in alkaline media [37, 38]. The optimal HEA/hNCNC catalyst exhibits excellent bifunctional activity and good stability for GOR and HER in alkaline medium, with an ultralow cell voltage of 0.373 V and a long-term stability over 50 h in glycerol-assisted water electrolysis. This study offers a versatile approach for developing bifunctional GOR and HER electrocatalysts, and demonstrates a viable low-energy strategy for electrochemical hydrogen production.

2 Results and discussion

The hNCNC has three-dimensional (3D) hierarchical structure with large specific surface area (1256 $m^2 \cdot g^{-1}$), high N content (6.6 at.%) and coexistence of micro-meso-macropores (Fig. S1 in the Electronic Supplementary Material (ESM)). HEA catalysts were prepared through impregnation-freeze drying followed by microwave treatment (Fig. S2 in the ESM). After the modified impregnation-freeze drying process, metal ions were uniformly dispersed on hNCNC without the observable nanoparticles/clusters (Fig. S3 in the ESM), due to the abundant micropores and N dopants on the hNCNC surface [39]. The morphological and structural characterizations of HEA/hNCNC are shown in Fig. 1. After the microwave heating, the HEA nanoparticles are highly dispersed on hNCNC, with an average particle size of 3.9 ± 1.8 nm. The lattice fringes with a spacing of 0.212 nm are clearly observed, showing high crystallization of the HEA nanoparticles (Fig. 1(a)). Three broad diffraction peaks appear at 40.8°, 47.2°, and 69.0° of the X-ray diffraction (XRD) pattern, which are different from the diffractions of pure Pt (PDF No. 04-0802), Rh (PDF No. 05-0685), Ru (PDF No. 06-0663), Cu (PDF No. 04-0836), Cr (PDF No. 06-0694), and Mn (PDF No. 32-0637), and can be assigned to the (111), (200), and (220) planes of face-centered cubic structure similar to metallic Pt (Fig. 1(b)). The electron-energy loss spectroscopy (EELS) element mappings display the homogeneous element mixing in the HEA nanoparticle (Fig. 1(c)). These results reflect the formation of single-phase PtRhRuCuCrMn HEA nanoparticles on the hNCNC support. The X-ray photoelectron spectroscopy (XPS) spectra indicate the existence of Pt, Rh, Ru, Cu, Cr, and Mn elements with both metallic and oxidation states (Fig. S4 in the ESM), and inductively coupled plasma-mass spectroscopy (ICP-MS) analysis gave their atomic ratio of 11.2:10.4:13.2:20.8:21.3:23.1 (Table S1 in the ESM). By comparing the XPS fine spectra of metals, it is learnt that the binding energies of Pt, Rh, Ru, and Mn in HEA/hNCNC are lower than those in HEA nanoparticles supported on hierarchical carbon nanocages

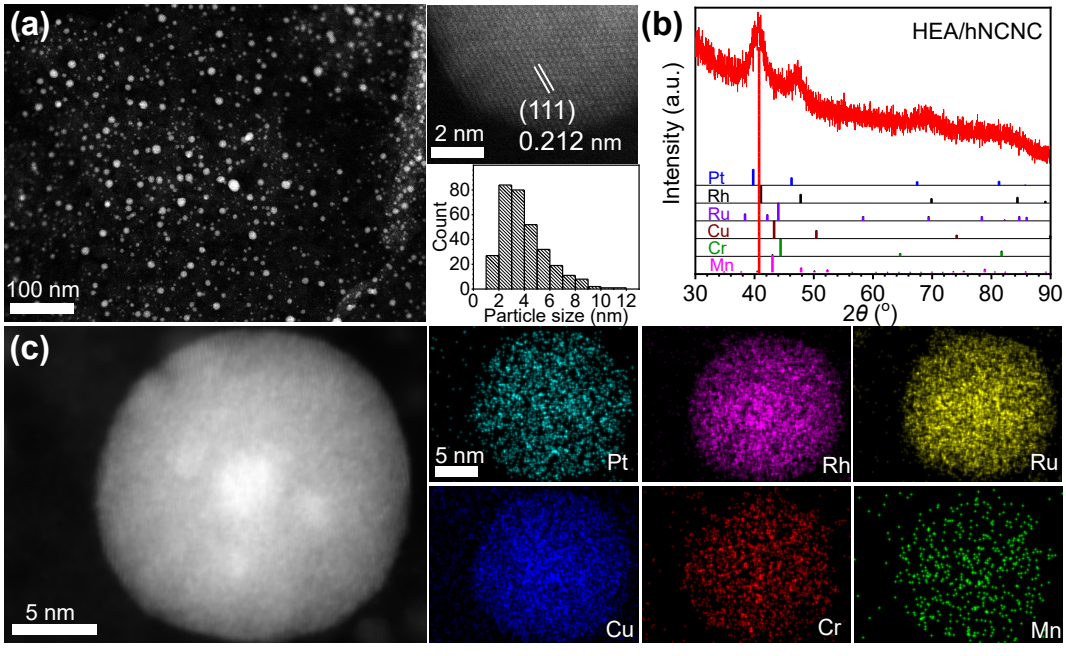

Figure 1 Morphology and structure of HEA/hNCNC. (a) High-angle annular dark-field scanning transmission electron microscope (HAADF-STEM) image. Insets in (a) are high-resolution image and size distribution histogram. (b) XRD pattern. (c) HAADF-STEM image and corresponding elemental mapping images.

(HEA/hCNC), which reveals the electron transfer from the N dopants of hNCNC to Pt, Rh, Ru, and Mn, indicating the stronger metal–support interaction for the former (Fig. S4 in the ESM). In addition, by comparing the Pt 4f spectra of HEA/hNCNC and Pt/hNCNC, the lower binding energy for HEA/hNCNC than Pt/hNCNC reflects the electron transfer from other metals to Pt, showing the electronic structure modulation of HEA (Fig. S5 in the ESM). Obviously, the N doping and high-entropy alloying markedly alter the electronic structure of Pt, which could regulate the adsorption of GOR intermediates on the catalyst surface, and thereby tune the electrocatalytic activity [27, 40]. The strong interaction between N dopants and metal species also promotes the high dispersion of HEA nanoparticles on the support (Fig. S6 in the ESM) and could further enhance the electrochemical stability of HEA/hNCNC [41].

The HEA/hNCNC was also prepared by using traditional high-temperature calcination method (Fig. S7 in the ESM), for comparison. XRD and ICP-MS analyses reveal that the prolonged high-temperature calcination readily induces metal loss and phase separation. Additionally, the traditional calcination method requires significantly higher energy and time consumption compared to the rapid microwave synthesis. More interestingly, the microwave synthesis can be extended to the preparation of HEAs with varied compositions, as well as ternary and quaternary alloys (Fig. S8 in the ESM). The rapid microwave synthesis strategy with convenience and general applicability is of significance for developing advanced HEA catalysts.

The GOR performances of HEA/hNCNC and control catalysts were evaluated in a three-electrode system, as shown in Fig. 2 (Fig. S9 in the ESM). The influence of glycerol concentration on GOR performance was investigated, revealing the optimal glycerol concentration of 0.6 mol·L^{-1} (Fig. S9(a) in the ESM). Among the series of alloy catalysts composed of 3–6 elements, the six-component PtRhRuCuCrMn alloy (i.e., HEA/hNCNC) exhibits the best GOR activity (Fig. S9(b) in the ESM), implying the important role of high-entropy effect in boosting the GOR performance. The linear sweep voltammetry (LSV) curves of HEA/hNCNC in 1 mol·L^{-1} KOH with or without 0.6 mol·L^{-1} glycerol indicate that the potential required to reach a current density of 10 mA·cm^{-2} is 1.335 V in the absence of glycerol, showing the decent OER activity; while this potential drastically decreases to 0.321 V in the presence of glycerol, indicating the more favorable GOR than OER on the HEA/hNCNC electrode (Fig. 2(a)). The Tafel slope for GOR (187.6 mV·dec^{-1}) is much lower than that for OER (267.7 mV·dec^{-1}), implying the faster reaction kinetics of GOR (Fig. 2(b)). The GOR performances of several commercial catalysts (Pt/C, Rh/C, and Ru/C) were also tested for comparison (Fig. S10 in the ESM). The Pt/C shows a lower peak mass activity (1.0 A·mg^{-1} at the peak potential of 1.15 V) and larger Tafel slope (209.3 mV·dec^{-1}) than that of the HEA/hNCNC (3.7 A·mg^{-1}@0.81 V and 187.6 mV·dec^{-1}). In contrast, the Rh/C and Ru/C catalysts exhibit negligible GOR performance, which indicates that the GOR activity of HEA/hNCNC mainly comes from the Pt species. After 60 h of chronopotentiometry (CP) measurement at a constant current density of 10 mA·cm^{-2}, the potential increases from 0.331 to 0.384 V (Fig. 2(c)), and the HEA nanoparticles are still uniformly distributed on hNCNC without agglomeration (Fig. S11(a) in the ESM), demonstrating the excellent stability of the HEA/hNCNC during GOR due to the strong HEA–support interaction (Fig. S4 in the ESM).

To unveil the rationale responsible for the superior GOR performance, CO stripping experiments were conducted to evaluate the anti-poisoning capabilities of HEA/hNCNC, with the results from commercial Pt/C, Rh/C, and Ru/C catalysts for comparison (Fig. 2(d)). The CO oxidation peak potentials are 0.627, 0.725, 0.685, and 0.704 V for HEA/hNCNC, Pt/C, Rh/C, and Ru/C, respectively, exhibiting the superior anti-poisoning ability of HEA/hNCNC. The better anti-poisoning capabilities of Rh/C and

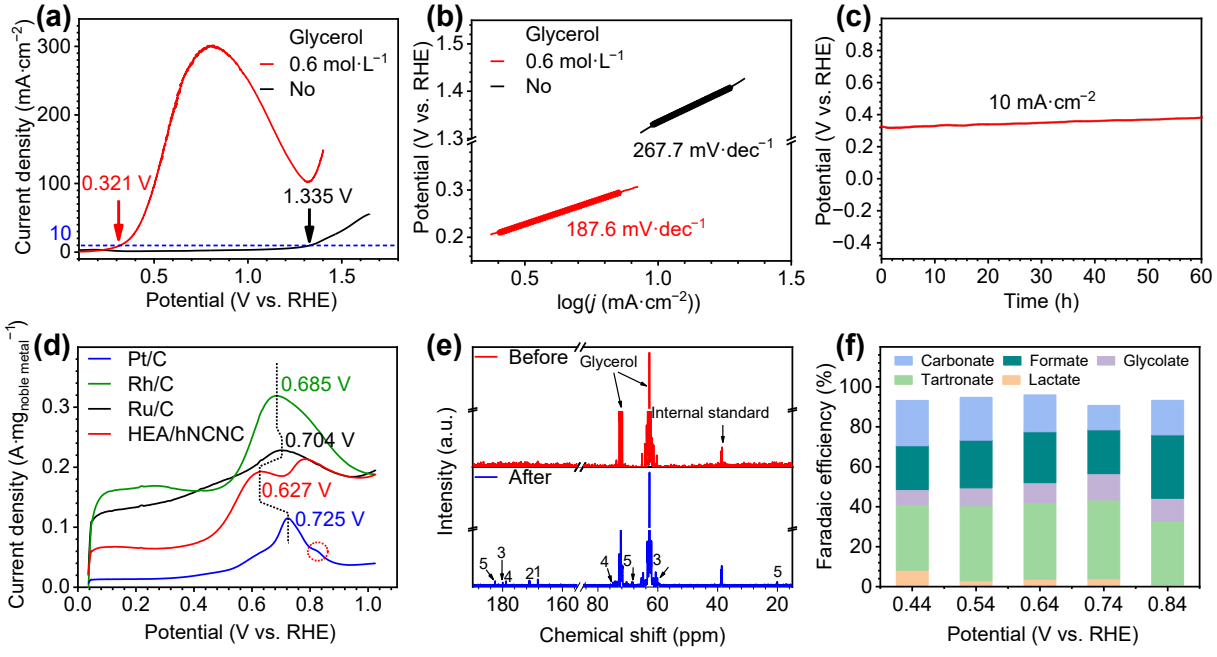

Figure 2 Anodic GOR performance of HEA/hNCNC. ((a) and (b)) LSV curves (a) and Tafel plots (b) of HEA/hNCNC in 1.0 mol·L^{-1} KOH with or without 0.6 mol·L^{-1} glycerol. (c) CP test at 10 mA·cm^{-2}. (d) Cyclic voltammetry curves of HEA/hNCNC, Pt/C, Rh/C, and Ru/C in CO stripping tests. (e) ^{13}C NMR spectra of electrolyte before and after 1 h test of GOR. (f) FE of GOR products. Note: In (d), the oxidation peaks at 0.78 V for HEA/hNCNC and 0.83 V for Pt/C (red dotted circle) could be attributed to the oxidation of Pt metal (Fig. S10(a) in the ESM). In (e), the numbers 1 to 5 represent carbonate, formate, glycolate, tartronate, and lactate.

Ru/C than Pt/C stem from their ability to provide adsorbed hydroxyl (OH_{ads}) species, thereby boosting the oxidation of adsorbed carbon monoxide (CO_{ads}) species to CO_2 [36, 42]. The superior anti-poisoning ability of HEA/hNCNC could be attributed to the fast oxidation of CO_{ads} into CO_2, facilitated by the weakened bonding strength of CO_{ads} on HEA due to the higher electron density of Pt in HEA/hNCNC (Figs. S4 and S5 in the ESM), and the abundant OH_{ads} intermediates generated by the Rh, Ru, and Mn species [40].

To understand the reaction pathway of GOR with the catalysis of HEA/hNCNC, the ^{13}C nuclear magnetic resonance (NMR) measurement was employed to analyze the GOR products (Figs. 2(e) and 2(f) and Figs. S11(b) and S11(c) in the ESM), which consist of CO_2, formic acid, glycolic acid, tartronic acid, and lactic acid, existing in the forms of corresponding salts in KOH electrolyte, i.e., carbonate, formate, glycolate, tartronate, and lactate, respectively (Fig. 2(e)). The HEA/hNCNC electrode achieves a high Faradaic efficiency (FE) of > 90% in a potential range from 0.44 to 0.84 V (Fig. 2(f)). The production of CO_2 indicates that partial glycerol experienced the complete oxidation, which benefits from the C–C bond cleavage functions of Rh and Cu in HEA/hNCNC [36, 43]. The reaction pathway of GOR mainly proceeds along Pathway A as depicted in Fig. S11(c) in the ESM, resulting in the production of dominant C_1 and C_2 products.

As a bifunctional catalyst, the HER performance of HEA/hNCNC was also evaluated, as shown in Fig. 3, with the performances of some alloy catalysts, commercial Pt/C, Rh/C, and Ru/C catalysts for comparison (Fig. S12 in the ESM). The HER polarization curves clearly show the best HER activity of HEA/hNCNC among these catalysts (Fig. 3(a) and Fig. S12 in the ESM). Specifically, the HEA/hNCNC presents much smaller overpotential (η_{10}: 20 mV@10 mA·cm^{-2}) and higher mass activity (2.28 A·mg^{-1}@50 mV) than that of Rh/C (43 mV, 0.78 A·mg^{-1}), Ru/C (52 mV, 0.67 A·mg^{-1}), and Pt/C (34 mV, 0.34 A·mg^{-1}) (Fig. 3(b)). The higher mass activity of HEA/hNCNC indicates the increased utilization of noble metals, implying the possibility of decreasing catalyst cost. The Tafel slopes are 38, 47, 52, and 52 mV·dec^{-1} for HEA/hNCNC, Rh/C, Ru/C, and Pt/C, respectively (Fig. 3(c)), indicating the faster HER kinetics of HEA/hNCNC than other catalysts [44]. The turnover frequency (TOF) values, the figure-of-merit to express the intrinsic activity of catalyst [45], of the four catalysts were also calculated according to the number of active sites (Fig. S13 in the ESM). The HEA/hNCNC has much larger TOF value than Rh/C, Ru/C, and Pt/C, indicating the high intrinsic activity of active sites in HEA/hNCNC (Fig. 3(d)). The remarkable HER electroactivity of HEA/hNCNC could be attributed to the highly exposed active sites of HEA nanoparticles and multiple active sites [28, 46].

The HER stability of HEA/hNCNC was assessed through 50 h CP test and a 5000-cycle accelerated degradation test. During the 50 h of CP testing at current densities of 10 and 100 mA·cm^{-2}, only a slight increase in overpotential was observed, from 20 to 25 mV and 52 to 78 mV, respectively (Fig. 3(e)). Additionally, little negative shift in overpotential can be observed on the LSV curves after 5000 cyclic voltammetry (CV) cycles (Fig. S14(a) in the ESM). The HEA nanoparticles exhibited uniform distribution with a maintained average particle size of 4.2 nm after the CP test at 10 mA·cm^{-2} (Fig. S14(b) in the ESM). These findings suggest the excellent HER stability of HEA/hNCNC owing to the high-entropy effect and strong HEA–support interaction [47, 48].

Prior to the utilization as bifunctional catalysts, the HER performance of HEA/hNCNC was assessed in 1.0 mol·L^{-1} KOH containing 0.6 mol·L^{-1} glycerol, considering that the presence of glycerol in the electrolyte could affect the HER performance (Fig. S15 in the ESM). In the single-chamber cell, the presence of glycerol in the electrolyte decreased the HER performance indeed, with a higher η_{10} overpotential of 41 mV and poorer stability. Even though the HEA/hNCNC exhibits excellent performance as bifunctional catalysts for GOR and HER in the glycerol-assisted hydrogen production, as shown in Fig. 4. A two-electrode electrolyzer was assembled with HEA/hNCNC serving as both anode and cathode catalysts, and 1.0 mol·L^{-1} KOH containing 0.6 mol·L^{-1} glycerol as the electrolyte (Fig. 4(a)). For comparison, a conventional overall water splitting test was conducted in the same electrolyzer without

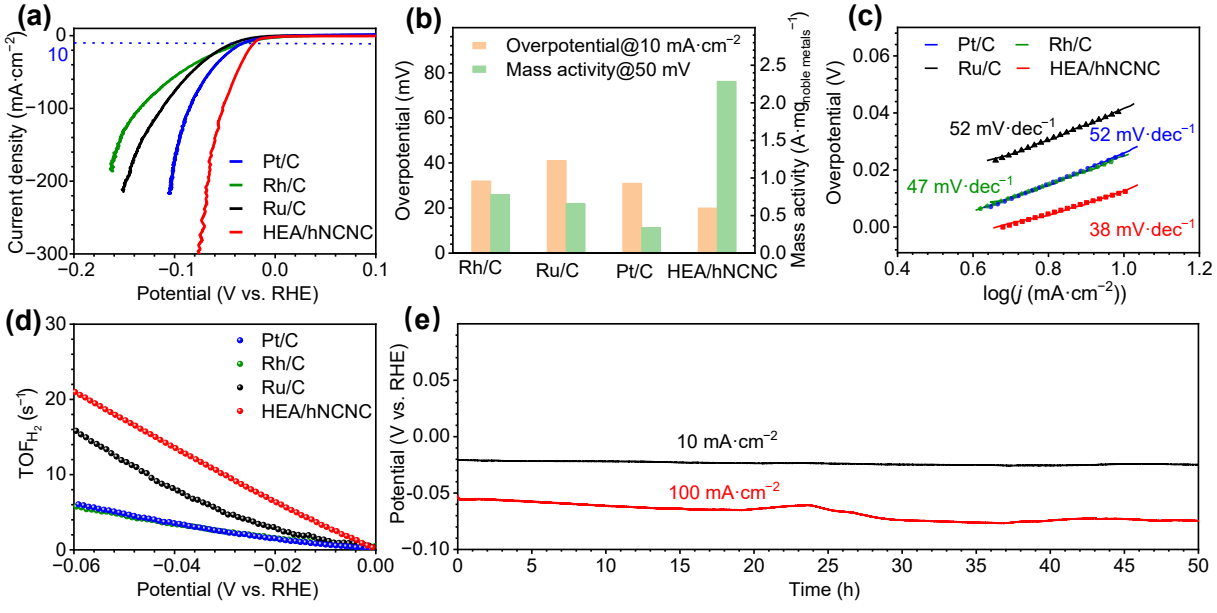

Figure 3 Cathodic HER performance of HEA/hNCNC and commercial catalysts in 1 mol·L^{-1} KOH. (a) LSV curves. (b) Overpotential at 10 mA·cm^{-2} and mass activity at 50 mV. (c) Tafel plots. (d) TOF curves. (e) CP test of HEA/hNCNC at 10 and 100 mA·cm^{-2}.

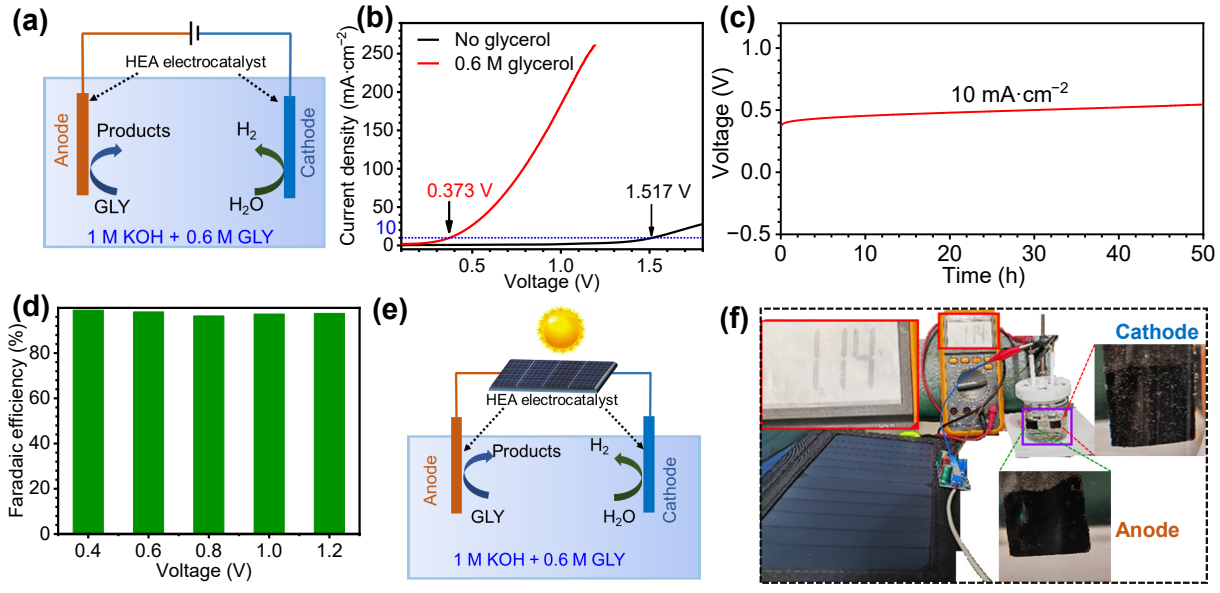

Figure 4 Electrochemical performance of single-chamber glycerol-assisted water electrolyzer. (a) Schematic illustration. (b) LSV curves in 1.0 mol·L^{-1} KOH solution with or without 0.6 mol·L^{-1} glycerol. (c) Stability at 10 mA·cm^{-2} in 1.0 mol·L^{-1} KOH containing 0.6 mol·L^{-1} glycerol. (d) FEs for H_2 at different voltages. ((e) and (f)) Schematic illustration and photograph of solar-driven glycerol-assisted water electrolyzer.

glycerol. The glycerol-assisted water electrolyzer requires an applied voltage of 0.373 V to reach a current density of 10 mA·cm^{-2}, significantly lower than the 1.517 V required in the conventional overall water electrolyzer (Fig. 4(b)). Such a low cell voltage is also notably lower than most previous studies for chemical-assisted water splitting (Tables S2 and S3 in the ESM). After 50 h CP test at 10 mA·cm^{-2}, the cell voltage slightly increases from 0.376 to 0.543 V, demonstrating good long-term durability (Fig. 4(c)). The FE for H_2 at different current densities remains nearly ~ 100% (Fig. 4(d) and Fig. S16 in the ESM).

In the double-chamber electrolyzer separated by anion-exchange membrane (Fig. S17(a) in the ESM), the glycerol-assisted hydrogen production of HEA/hNCNC was also conducted, which demonstrates inferior performance in comparison to that in the single-chamber electrolyzer (Fig. S17(b) in the ESM and Fig. 4(b)). It could be attributed to the sluggish ion (OH^-) transport caused by anion-exchange membrane. Despite the detrimental effect of glycerol on the HER, the single-chamber electrolyzer is more rational than the double-chamber configuration, which highlights the benefit of bifunctional catalyst.

As is known, H_2 serves as an efficient carrier for storing intermittent solar energy [49]; hence the demonstration of a solar-driven glycerol-assisted water electrolyzer was performed (Figs. 4(d) and 4(e)). At a potential of 1.14 V powered by a solar cell, the continuous generation of H_2 bubbles was observed on the cathode, while no bubbles were detected on the anode. This result indicates the promising application of HEA/hNCNC in solar-driven glycerol-assisted water electrolyzer to produce H_2.

3 Conclusions

In summary, hNCNC supported PtRhRuCuCrMn HEA catalysts have been prepared through a facile and rapid microwave method. In alkaline media, the optimized HEA/hNCNC catalyst exhibits excellent bifunctional activity for both GOR and HER, along with good stability. The high-entropy compositional design promotes the C–C cleavage and anti-poisoning capability for GOR, while providing multi-active sites for HER. The N-participation ensures the high dispersion of HEA nanoparticles and high stability for both GOR and HER. Thanks to the contribution from the excellent electrocatalytic performances for GOR and HER, the assembled electrolyzer only requires a low cell voltage of 0.373 V to afford the current density of 10 mA·cm^{-2}, which reduces the voltage input by 1.144 V compared to conventional water splitting. It also maintains long-term stability over 50 h with nearly 100% FE for H_2. More importantly, the H_2 production through glycerol-assisted water electrolysis was driven by solar cell, showing great potential in practical applications. This study provides a promising bifunctional electrocatalyst for GOR and HER, and suggests an energy-efficient hydrogen generation approach by glycerol-assisted water electrolysis.

Electronic Supplementary Material: Supplementary material (material synthesis and characterization, electrochemical measurements, product quantification, and calculation of the turnover frequency and Faradaic efficiency) is available in the online version of this article at https://doi.org/10.26599/NR.2026.94908651.

Data availability

All data needed to support the conclusions in the paper are presented in the manuscript and the Electronic Supplementary Material. Additional data related to this paper may be requested from the corresponding author upon request.

Acknowledgements

We appreciate the jointly financial supports from the National Key Research and Development Program of China (Nos. 2021YFA1500900 and 2024YFA1208900), the National Natural Science Foundation of China (Nos. 22479073 and 22475097), the Major Science and Technology Projects of Jiangsu Province (No. BG2024033), the Science and Technology Research Project of

Jiangxi Provincial Department of Education (No. GJJ2400713), and the Jiangxi University of Science and Technology University-Level Vertical Research Project (No. jxust-16).

Declaration of competing interest

All the contributing authors report no conflict of interests in this work.

Author contribution statement

J. T. J.: Conceptualization, data curation, formal analysis, writing – original draft. F. F. X.: Investigation, methodology. W. Z. Z.: Data curation. Z.C.: Formal analysis. X. Q. W.: Formal analysis. X. Y. L.: Visualization. L. J. Y.: Supervision. Q. W.: Conceptualization, supervision, writing – review & editing. X. Z. W.: Conceptualization, writing – review & editing. Z. H.: Resources, funding acquisition. All the authors have approved the final manuscript.

Use of AI statement

None.

References

[1] Slobodkin, I.; Davydova, E.; Sananis, M.; Breytus, A.; Rothschild, A. Electrochemical and chemical cycle for high-efficiency decoupled water splitting in a near-neutral electrolyte. *Nat. Mater.* **2024**, *23*, 398–405.

[2] Tüysüz, H. Alkaline water electrolysis for green hydrogen production. *Acc. Chem. Res.* **2024**, *57*, 558–567.

[3] Chen, Q.; Wei, B.; Wei, Y.; Zhai, P. B.; Liu, W.; Gu, X. K.; Yang, Z. L.; Zuo, J. H.; Zhang, R. F.; Gong, Y. J. Synergistic effect in ultrafine PtNiP nanowires for highly efficient electrochemical hydrogen evolution in alkaline electrolyte. *Appl. Catal. B: Environ.* **2022**, *301*, 120754.

[4] Sun, Y.; Zang, Y. P.; Tian, W. Z.; Yu, X. J.; Qi, J. Z.; Chen, L. W.; Liu, X.; Qiu, H. B. Plasma-induced large-area N, Pt-doping and phase engineering of MoS_2 nanosheets for alkaline hydrogen evolution. *Energy Environ. Sci.* **2022**, *15*, 1201–1210.

[5] Niu, F.; Wu, Z. Q.; Chen, D.; Huang, Y. X.; Ordomsky, V. V.; Khodakov, A. Y.; Van Geem, K. M. State-of-the-art and perspectives of hydrogen generation from waste plastics. *Chem. Soc. Rev.* **2025**, *54*, 4948–4972.

[6] Zhao, Z. F.; Shen, X. Y.; Luo, X. Y.; Chen, M. H.; Zhang, M. D.; Yu, R. P.; Jin, R. T.; Zheng, H. J. Electric field redistribution triggered surface adsorption and mass transfer to boost electrocatalytic glycerol upgrading coupled with hydrogen evolution. *Adv. Energy Mater.* **2024**, *14*, 2400851.

[7] Wang, P.; Zheng, J.; Xu, X.; Zhang, Y. Q.; Shi, Q. F.; Wan, Y.; Ramakrishna, S.; Zhang, J.; Zhu, L. Y.; Yokoshima, T. et al. Unlocking efficient hydrogen production: Nucleophilic oxidation reactions coupled with water splitting. *Adv. Mater.* **2024**, *36*, 2404806.

[8] Yao, H.; Zheng, Y. N.; Yu, X.; Hu, S. J.; Su, B. L.; Guo, X. H. Rational modulation of electronic structure in PtAuCuNi alloys boosts efficient electrocatalytic ethanol oxidation assisted with energy-saving hydrogen evolution. *J. Energy Chem.* **2024**, *93*, 557–567.

[9] Li, Z. H.; Yan, Y. F.; Xu, S. M.; Zhou, H.; Xu, M.; Ma, L. N.; Shao, M. F.; Kong, X. G.; Wang, B.; Zheng, L. R. et al. Alcohols electrooxidation coupled with H_2 production at high current densities promoted by a cooperative catalyst. *Nat. Commun.* **2022**, *13*, 147.

[10] Zhai, J. X.; Wang, Z. R.; Cao, X. J.; Zhao, Y. L.; Lu, Z. Y.; He, P. L. Regulating the electronic structure of nickel phosphides via interface engineering and molybdenum doping boosts benzyl alcohol oxidation coupled with hydrogen production. *Chem. Eng. J.* **2024**, *499*, 156646.

[11] Shi, Z. K.; Zhang, Y.; Guo, W.; Niu, Z. H.; Chen, Y.; Huang, J. L. Self-encapsulated Ni nanoparticles on delignified wood carbon for efficient urea-assisted hydrogen production. *Adv. Funct. Mater.* **2025**, *35*, 2414935.

[12] Wang, T. Z.; Miao, L. C.; Zheng, S. Y.; Qin, H. Y.; Cao, X. J.; Yang, L.; Jiao, L. F. Interfacial engineering of Ni_3N/Mo_2N heterojunctions for urea-assisted hydrogen evolution reaction. *ACS Catal.* **2023**, *13*, 4091–4100.

[13] Shi, M. J.; Sultana, F.; Qin, X. J.; Zhang, P.; Qian, K. C.; Wei, T.; Duan, Y.; Li, T. T.; Bai, J. M.; Li, R. H. *In situ* evolution of MOF-derived C@NiCoP/NF promotes urea-assisted electrocatalytic hydrogen production. *Appl. Catal. B: Environ. Energy* **2025**, *371*, 125210.

[14] Huang, Y.; Chong, X. D.; Liu, C. B.; Liang, Y.; Zhang, B. Boosting hydrogen production by anodic oxidation of primary amines over a NiSe nanorod electrode. *Angew. Chem., Int. Ed.* **2018**, *57*, 13163–13166.

[15] Zhang, J. Y.; Wang, H. M.; Tian, Y. F.; Yan, Y.; Xue, Q.; He, T.; Liu, H. F.; Wang, C. D.; Chen, Y.; Xia, B. Y. Anodic hydrazine oxidation assists energy-efficient hydrogen evolution over a bifunctional cobalt perselenide nanosheet electrode. *Angew. Chem., Int. Ed.* **2018**, *57*, 7649–7653.

[16] Tang, W. S.; Zhang, L. N.; Qiu, T. Y.; Tan, H. Q.; Wang, Y. H.; Liu, W.; Li, Y. G. Efficient conversion of biomass to formic acid coupled with low energy consumption hydrogen production from water electrolysis. *Angew. Chem., Int. Ed.* **2023**, *62*, e202305843.

[17] Wu, J. X.; Liu, X.; Hao, Y. M.; Wang, S. Y.; Wang, R.; Du, W.; Cha, S. S.; Ma, X. Y.; Yang, X. J.; Gong, M. Ligand hybridization for electro-reforming waste glycerol into isolable oxalate and hydrogen. *Angew. Chem., Int. Ed.* **2023**, *62*, e202216083.

[18] Qian, Q. Z.; He, X. Y.; Li, Z. Y.; Chen, Y. X.; Feng, Y. F.; Cheng, M. Y.; Zhang, H. K.; Wang, W. T.; Xiao, C.; Zhang, G. Q.et al. Electrochemical biomass upgrading coupled with hydrogen production under industrial-level current density. *Adv. Mater.* **2023**, *35*, 2300935.

[19] Han, X. T.; Sheng, H. Y.; Yu, C.; Walker, T. W.; Huber, G. W.; Qiu, J. S.; Jin, S. Electrocatalytic oxidation of glycerol to formic acid by $CuCo_2O_4$ spinel oxide nanostructure catalysts. *ACS Catal.* **2020**, *10*, 6741–6752.

[20] Balog, Á.; Kecsenovity, E.; Samu, G. F.; He, J.; Fekete, D.; Janáky, C. Paired photoelectrochemical conversion of CO_2/H_2O and glycerol at high rate. *Nat. Catal.* **2024**, *7*, 522–535.

[21] Andrei, V.; Roh, I.; Lin, J. A.; Lee, J.; Shan, Y.; Lin, C. K.; Shelton, S.; Reisner, E.; Yang, P. D. Perovskite-driven solar C_2 hydrocarbon synthesis from CO_2. *Nat. Catal.* **2025**, *8*, 137–146.

[22] Du, H. Y.; Wang, K.; Tsiakaras, P.; Shen, P. K. Excavated and dendritic Pt–Co nanocubes as efficient ethylene glycol and glycerol oxidation electrocatalysts. *Appl. Catal. B: Environ.* **2019**, *258*, 117951.

[23] Yang, F.; Ye, J. Y.; Yuan, Q.; Yang, X. T.; Xie, Z. X.; Zhao, F. L.; Zhou, Z. Y.; Gu, L.; Wang, X. Ultrasmall Pd–Cu–Pt trimetallic twin icosahedrons boost the electrocatalytic performance of glycerol oxidation at the operating temperature of fuel cells. *Adv. Funct. Mater.* **2020**, *30*, 1908235.

[24] Chen, W.; Zhang, L.; Xu, L. T.; He, Y. Q.; Pang, H.; Wang, S. Y.; Zou, Y. Q. Pulse potential mediated selectivity for the electrocatalytic oxidation of glycerol to glyceric acid. *Nat. Commun.* **2024**, *15*, 2420.

[25] Yao, Y. G.; Dong, Q.; Brozena, A.; Luo, J.; Miao, J. W.; Chi, M. F.; Wang, C.; Kevrekidis, I. G.; Ren, Z. J.; Greeley, J. et al. High-entropy nanoparticles: Synthesis–structure–property relationships and data-driven discovery. *Science* **2022**, *376*, eabn3103.

[26] Liang, J. J.; Cao, G. H.; Zeng, M. Q.; Fu, L. Controllable synthesis of high-entropy alloys. *Chem. Soc. Rev.* **2024**, *53*, 6021–6041.
[27] Chen, W.; Luo, S. P.; Sun, M. Z.; Wu, X. Y.; Zhou, Y. S.; Liao, Y. J.; Tang, M.; Fan, X. K.; Huang, B. L.; Quan, Z. W. High-entropy intermetallic PtRhBiSnSb nanoplates for highly efficient alcohol oxidation electrocatalysis. *Adv. Mater.* **2022**, *34*, 2206276.
[28] Li, H. D.; Han, Y.; Zhao, H.; Qi, W. J.; Zhang, D.; Yu, Y. D.; Cai, W. W.; Li, S. X.; Lai, J. P.; Huang, B. L. et al. Fast site-to-site electron transfer of high-entropy alloy nanocatalyst driving redox electrocatalysis. *Nat. Commun.* **2020**, *11*, 5437.
[29] Wei, M.; Sun, Y. Y.; Zhang, J. Y.; Ai, F.; Xi, S. B.; Wang, J. K. High-entropy alloy nanocrystal assembled by nanosheets with d–d electron interaction for hydrogen evolution reaction. *Energy Environ. Sci.* **2023**, *16*, 4009–4019.
[30] Wang, C. H.; Zhang, J.; Miao, K. H.; Long, M. R.; Lai, S. Y.; Zhao, S. J.; Kang, X. W. Octahedral nanocrystals of Ru-doped PtFeNiCuW/CNTs high-entropy alloy: High performance toward pH-universal hydrogen evolution reaction. *Adv. Mater.* **2024**, *36*, 2400433.
[31] Xin, Y.; Li, S. H.; Qian, Y. Y.; Zhu, W. K.; Yuan, H. B.; Jiang, P. Y.; Guo, R. H.; Wang, L. B. High-entropy alloys as a platform for catalysis: Progress, challenges, and opportunities. *ACS Catal.* **2020**, *10*, 11280–11306.
[32] Li, H. D.; Lai, J. P.; Li, Z. J.; Wang, L. Multi-sites electrocatalysis in high-entropy alloys. *Adv. Funct. Mater.* **2021**, *31*, 2106715.
[33] Qiao, H. Y.; Saray, M. T.; Wang, X. Z.; Xu, S. M.; Chen, G.; Huang, Z. N.; Chen, C. J.; Zhong, G.; Dong, Q.; Hong, M. et al. Scalable synthesis of high entropy alloy nanoparticles by microwave heating. *ACS Nano* **2021**, *15*, 14928–14937.
[34] Zhao, H.; Zhang, D.; Yuan, Y. Y.; Wu, X. K.; Li, S. X.; Li, Z. J.; Lai, J. P.; Wang, L. Rapid and large-scale synthesis of ultra-small immiscible alloy supported catalysts. *Appl. Catal. B: Environ.* **2022**, *304*, 120916.
[35] Zhao, H. Y.; Song, B. B.; Li, H.; Li, X. Y.; Ge, C.; Wu, Q. L.; Chen, J.; Wang, Z.; Yan, G. L.; Fang, J. Controllable microwave heating for energy-efficient and universal synthesis of atomically dispersed metals on nitrogen-doped carbon nanofibers. *Small* **2025**, *21*, 2407700.
[36] Zhu, Y. M.; Bu, L. Z.; Shao, Q.; Huang, X. Q. Subnanometer PtRh nanowire with alleviated poisoning effect and enhanced C–C bond cleavage for ethanol oxidation electrocatalysis. *ACS Catal.* **2019**, *9*, 6607–6612.
[37] Huang, Z. L.; Hu, S. N.; Sun, M. Z.; Xu, Y.; Liu, S. H.; Ren, R. J.; Zhuang, L.; Chan, T. S.; Hu, Z. W.; Ding, T. Y. et al. Implanting oxophilic metal in PtRu nanowires for hydrogen oxidation catalysis. *Nat. Commun.* **2024**, *15*, 1097.
[38] Kim, J.; Jung, H.; Jung, S. M.; Hwang, J.; Kim, D. Y.; Lee, N.; Kim, K. S.; Kwon, H.; Kim, Y. T.; Han, J. W. et al. Tailoring binding abilities by incorporating oxophilic transition metals on 3D nanostructured Ni arrays for accelerated alkaline hydrogen evolution reaction. *J. Am. Chem. Soc.* **2020**, *143*, 1399–1408.
[39] Zhang, Z. Q.; Chen, Y. G.; Zhou, L. Q.; Chen, C.; Han, Z.; Zhang, B. S.; Wu, Q.; Yang, L. J.; Du, L. Y.; Bu, Y. F. et al. The simplest construction of single-site catalysts by the synergism of micropore trapping and nitrogen anchoring. *Nat. Commun.* **2019**, *10*, 1657.
[40] Chang, J. F.; Wang, G. Z.; Li, C.; He, Y. Q.; Zhu, Y. M.; Zhang, W.; Sajid, M.; Kara, A.; Gu, M.; Yang, Y. Rational design of septenary high-entropy alloy for direct ethanol fuel cells. *Joule* **2023**, *7*, 587–602.
[41] Kuang, P. Y.; Wang, Y. R.; Zhu, B. C.; Xia, F. J.; Tung, C. W.; Wu, J. S.; Chen, H. M.; Yu, J. G. Pt single atoms supported on N-doped mesoporous hollow carbon spheres with enhanced electrocatalytic H_2-evolution activity. *Adv. Mater.* **2021**, *33*, 2008599.
[42] Huang, L.; Sun, J. Y.; Cao, S. H.; Zhan, M.; Ni, Z. R.; Sun, H. J.; Chen, Z.; Zhou, Z. Y.; Sorte, E. G.; Tong, Y. J. et al. Combined EC-NMR and *in situ* FTIR spectroscopic studies of glycerol electrooxidation on Pt/C, PtRu/C, and PtRh/C. *ACS Catal.* **2016**, *6*, 7686–7695.
[43] Peng, H. C.; Ren, J.; Wang, Y. C.; Xiong, Y.; Wang, Q. C.; Li, Q.; Zhao, X.; Zhan, L. S.; Zheng, L. R.; Tang, Y. G. et al. One-stone, two birds: Alloying effect and surface defects induced by Pt on $Cu_{2-x}Se$ nanowires to boost C–C bond cleavage for electrocatalytic ethanol oxidation. *Nano Energy* **2021**, *88*, 106307.
[44] Tan, H.; Tang, B.; Lu, Y.; Ji, Q. Q.; Lv, L. Y.; Duan, H. L.; Li, N.; Wang, Y.; Feng, S. H.; Li, Z. et al. Engineering a local acid-like environment in alkaline medium for efficient hydrogen evolution reaction. *Nat. Commun.* **2022**, *13*, 2024.
[45] Zheng, Y.; Jiao, Y.; Zhu, Y. H.; Li, L. H.; Han, Y.; Chen, Y.; Jaroniec, M.; Qiao, S. Z. High electrocatalytic hydrogen evolution activity of an anomalous ruthenium catalyst. *J. Am. Chem. Soc.* **2016**, *138*, 16174–16181.
[46] Yao, R. Q.; Zhou, Y. T.; Shi, H.; Wan, W. B.; Zhang, Q. H.; Gu, L.; Zhu, Y. F.; Wen, Z.; Lang, X. Y.; Jiang, Q. Nanoporous surface high-entropy alloys as highly efficient multisite electrocatalysts for nonacidic hydrogen evolution reaction. *Adv. Funct. Mater.* **2021**, *31*, 2009613.
[47] Qiao, Z.; Hwang, S.; Li, X.; Wang, C. Y.; Samarakoon, W.; Karakalos, S.; Li, D. G.; Chen, M. J.; He, Y. H.; Wang, M. Y. et al. 3D porous graphitic nanocarbon for enhancing the performance and durability of Pt catalysts: A balance between graphitization and hierarchical porosity. *Energy Environ. Sci.* **2019**, *12*, 2830–2841.
[48] Feng, G.; Ning, F. H.; Song, J.; Shang, H. F.; Zhang, K.; Ding, Z. P.; Gao, P.; Chu, W. S.; Xia, D. G. Sub-2 nm ultrasmall high-entropy alloy nanoparticles for extremely superior electrocatalytic hydrogen evolution. *J. Am. Chem. Soc.* **2021**, *143*, 17117–17127.
[49] Zhang, J.; Zhang, Q. Y.; Feng, X. L. Support and interface effects in water-splitting electrocatalysts. *Adv. Mater.* **2019**, *31*, 1808167.